1997AJ....113.2147H

THE ASTRONOMICAL JOURNAL VOLUME 113, NUMBER 6 JUNE 1997

HIGH-RESOLUTION IMAGERY OF BD +30°3639 AND ITS DUSTY HALO

J. PATRICK HARRINGTON, NANCY JOANNE LAME, AND STEPHEN M. WHITE
Department of Astronomy, University of Maryland, College Park, Maryland 20742
Electronic mail: jph@astro.umd.edu

KAZIMIERZ J. BORKOWSKI
Department of Physics, North Carolina State University, Raleigh, North Carolina 27695
Electronic mail: kazik@mozart.physics.ncsu.edu

Received 1996 August 21; revised 1997 February 20

ABSTRACT

The planetary nebula BD +30°3639 has been imaged by the *Hubble Space Telescope* through nine narrow-band filters. A high-resolution radio map has been obtained with the VLA. Comparison of Hβ, Hα, and radio images allow us to derive the point-to-point variations in both the extinction and the ratio of total to selective absorption. The extinction shows (1) a gradient across the nebula, and (2) a large dust clump in the northeast and many small ($\sim$0.″2) dust features. The ratio of total to selective absorption for this nebula is close to the normal ISM value, and can be modeled by a power law distribution of amorphous carbon grains. It is found that the optical images show a substantial halo due to light scattered by dust in the neutral envelope surrounding the ionized shell. Monte Carlo models indicate that such scattering could result from a dust halo with an optical depth of unity and an albedo of $\sim$0.4. Such a high albedo is not consistent with pure carbon dust models. The halo images in [O I] λ6300 and [S II] λ6717,31 show anomalous structures not seen in the other lines, which seem to be in emission. The strongest [O I] feature is coincident with halo emission previously observed in the 1–0 $S(1)$ transition of H_2. The [O I] and [S II] emission may indicate shock heating of the halo. © *1997 American Astronomical Society.* [S0004-6256(97)00406-8]

1. INTRODUCTION

BD +30°3639, quaintly known as "Campbell's hydrogen-envelope star" (Campbell 1894), is one of the best studied planetary nebulae (PNe). It is a dense, ionization-bounded, presumably young nebula with a bright, WC9 Wolf-Rayet type central star. It is one of the few PNe whose distance has been determined by direct measurement of its angular expansion (Hajian *et al.* 1993; Kawamura & Mason 1996). Because it was identified as a *ROSAT* X-ray source with a spectrum which could be fit by thermal bremsstrahlung with a temperature of 3×10^6 K (Kreysing *et al.* 1992), a temperature too high to be attributed to the central star, it seemed likely that the X-rays originated in a bubble of shocked stellar wind filling the interior of the nebula. In order to learn more about the nature of the X-ray emitting gas we observed BD +30°3639 with the *Advanced Satellite for Cosmology and Astrophysics* (*ASCA*) and with the Wide Field Planetary Camera 2 (WFPC2) aboard the *Hubble Space Telescope* (*HST*). The results of these observations as they relate to the X-ray emission from this nebula have been described by Arnaud *et al.* (1996). Examination of the *HST* images, however, revealed a great deal of information regarding the dust in the nebula and in its neutral halo; that is the subject of this paper.

2. OBSERVATIONS

2.1 *HST WFPC2 Images and Optical Fluxes*

BD+30 was imaged in the lines of Hβ, Hα, He I λ5876, [O III] λ5007, [O II] λ3727, [O I] λ6300, [N II] λ6584, [S III] λ9539, and [S II] λ6717+6731 in 1994 March using the *HST* WFPC2 (Table 1). The nebula was positioned entirely on the high-resolution PC CCD chip of the WFPC2, which has a spatial resolution of 0.0455 arcsec/pixel.

The image processing and data reduction procedure followed standard techniques using NOAO's IRAF as well as various IDL procedures. The data reduction process included the *HST* pipeline processing (at STScI), cosmic ray cleaning, background subtraction and image registration. The final images for each emission line (except for Hβ, which is similar to Hα) are shown in Figs. 1(a)–1(h) (Plate 43). The images have all been rotated so that north is up and east is to the left.

The intensity scale in Fig. 1 is linear, so that details in the bright shell are seen clearly. The bright shell is seen to be rather narrow ($\sim$0.″6). It is not a smooth ellipse, but has a "squared off" shape which broadens and becomes rather diffuse in the southwest quadrant. Because the star is relatively cool (30,000 K: Preite-Martinez & Pottasch 1983) He^+ and O^{++} do not fill the entire H^+ zone. The resulting ionization stratification can be seen in the He I and [O III] images, where the main shell is thinner, and the fine structure

© American Astronomical Society • Provided by the NASA Astrophysics Data System

1997AJ....113.2147H

TABLE 1. List of observations.

Line	Filter	#	Exp.[a]	phot F_λ[b]
Hβ	F487N	1	600 s	6.979e13
Hα	F656N	1	200 s	2.342e14
He I λ5876	F588N	1	600 s	2.320e14
[O III] λ5007	F502N	1	600 s	8.699e13
[O II] λ3727	F375N	1	600 s	8.982e12
[O I] λ6300	F631N	2	500 s	2.493e14
[N II] λ6584	F658N	1	200 s	2.361e14
[S III] λ9532	F953N	2	400 s	5.635e13
[S II] λ6724	F673N	2	400 s	2.550e14

[a]Exposure time of final (averaged) image.
[b]Calculated with IRAF synphot.calcphot task.

seen in the interior is more pronounced than in the other images.

The small light patches seen particularly in the north and northeast sections of the shell are clearly due to extinction by dust—they are least prominent at the longest wavelength, [S III] λ9532, and are most noticeable in [O II] λ3727. Since BD+30 is known to have an extensive neutral envelope, these clumps may be outside the ionized shell, seen in projection.

A faint optical halo, extending to about 4″, can be seen in many of the emission lines in Fig. 1. It is more clearly seen in the Hα contour plot shown in Fig. 2. Because it is located close to the bright shell, the optical halo does not seem to have attracted much attention. Balick *et al.* (1992) did not detect it in their search for large, faint halos. Graham *et al.* (1993) remark "... although many planetary nebulae have faint shells and halos extending beyond the high surface brightness core, BD +30°3639 and NGC 7027 do not." While Bachiller *et al.* (1991) note that the optical images of

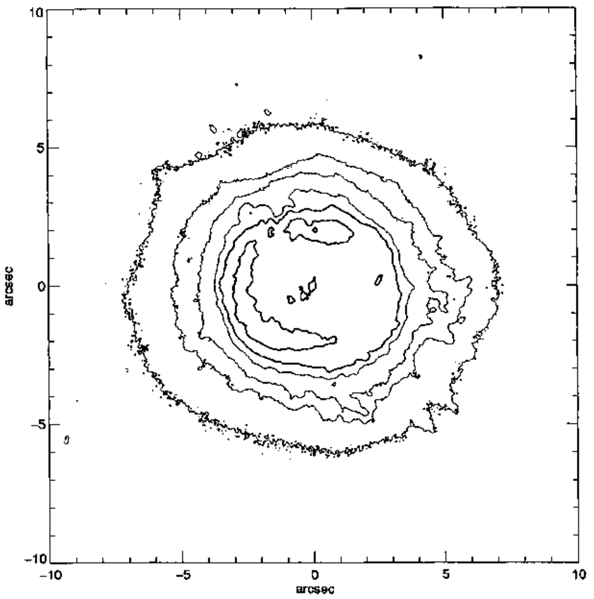

FIG. 2. Contour plot of the Hα image. The axes are labeled in arcsec. The contour levels are 1.0×10^{-13}, 5.0×10^{-13}, 1.0×10^{-12}, 2.5×10^{-12}, 5.46×10^{-12}, and 2.5×10^{-11} erg cm^{-2} s^{-1} arcsec^{-2}. North is up and east is to the left.

Balick (1987) "... show weak, more extended (10″) emission," they seem to regard this emission as ionized gas.

A number of arguments indicate that this halo is primarily due to scattered light. Because there is no evidence of radio emission beyond the bright shell, there cannot be much ionized gas there. The Hβ/Hα ratio increases in the halo, as would be expected for scattering (this effect is modeled in detail in Sec. 4). BD+30 is a dense, young nebula, so a neutral halo is not unexpected. The existence of this halo has been established by observations of H_2 emission (Graham *et al.* 1993), CO emission (Bachiller *et al.* 1991), and the 21 cm line of H I in both emission and absorption (Taylor *et al.* 1990), as well as by observations of the Na I resonance lines (which appear in absorption against the star but in emission 3″.5 away from it: Dinerstein & Sneden 1988). The CO, H I, and Na I observations suggest that the mass of the neutral halo is comparable to that of the ionized gas. Dust mixed with this neutral gas must scatter light from the core.

The IRAF "SYNPHOT" package was used for flux calibration. Flux calibration factors were determined with the "CALCPHOT" task, using recent filter transmission tables (dated 1995 June 12) over a finely gridded wavelength table. The date of the observations (1994 March) was explicitly input to the calcphot task to force the correct CCD temperature (which was changed subsequent to these observations). The output of the calcphot task was the expected counts for a 1 erg s^{-1} cm^{-2} flux; thus to convert counts to flux, the measured counts in the image should be divided by the phot F_λ factor given in Table 1.

Some of the pixels in the Hα image are saturated, and we estimate that the amount of flux missing from the Hα image is ~1.5% of the total flux. The raw Hα image has 604 pixels at 4096 DN, which is the limit of the A/D converter. Since the spatial variation in the Hα/Hβ ratio map is smoother than in the Hα emission image, we interpolated over the ratio map to estimate the flux in each of the saturated pixels. The [N II] image is also saturated, in approximately the same set of pixels as in the Hα image, but the "missing light" cannot be determined as for Hα.

The Hα image must be corrected for contamination by [N II]. While the F656N filter has a transmission of 4% at λ6584, a more serious effect is the 29% transmission at [N II] λ6548. Since the λ6548 line is 1/3 the strength of [N II] λ6584, the combined effect is equivalent to a 14% contamination by λ6584. In this nebula, the [N II] λ6584 flux is about equal to that of Hα, so this correction results in a 14% reduction in the Hα flux. There is also a corresponding leak by the [N II] F658N filter at λ6563, resulting in an ~4% reduction in the [N II] λ6584 flux.

To obtain accurate totals, the flux in each image was integrated over a circular aperture of 6″.6 (145 pixels) radius, which includes the halo. The central star flux was removed by excluding pixels with radius $r<7$ pixels. The integrated fluxes are listed in Table 2.

The flux calibrations for the *HST* images are claimed to have an accuracy of ~5% for stellar (continuum) sources (Holtzman *et al.* 1995). Flux calibrations with emission line sources have not been carried out and thus rest on the prelaunch filter transmission curves. This is especially worri-

© American Astronomical Society • Provided by the NASA Astrophysics Data System

TABLE 2. Fluxes from WFPC2 images.

Line	λ	Total flux[a]	Shell flux	Halo flux	Halo/shell
Hβ	4861	1.05e-10	8.88e-11	1.60e-11	0.180
Hα	6563	4.24e-10	3.64e-10	6.01e-11	0.165
He I	5876	1.36e-11	1.17e-11	1.94e-12	0.167
[O III]	5007	9.45e-12	8.06e-12	1.39e-12	0.173
[O II]	3727	8.62e-11	6.78e-11	1.84e-11	0.271
[O I]	6300	8.64e-12	6.89e-12	1.75e-12	0.253
[N II]	6584	4.57e-10	3.88e-10	6.93e-11	0.179
[S III]	9539	1.75e-10	1.55e-10	2.01e-11	0.129
[S II]	6724	2.93e-11	2.33e-11	6.03e-12	0.259

[a]Integrated over a circular aperture of 6.″6 (145 pixels) radius.

some with regard to the correction applied to the Hα flux for the [N II] doublet, since the [N II] lines lie on the steep shoulders of the filter passband. An additional problem is a possible few percent contamination by the stellar continuum scattered by dust in the halo and in the ionized shell. Thus it is important to compare our results with ground-based observations. The classic measurements are O'Dell & Terzian (1970) who give $\log F(\mathrm{H}\beta) = -10.01 \pm 0.03$, and Peimbert & Torres-Peimbert (1971) who found $\log F(\mathrm{H}\beta) = -10.00$. The mean of these values, after correction by -0.03 dex for the recalibration of Vega (Hayes & Lantham 1975), yields 9.23×10^{-11} ergs cm^{-2} s^{-1}, 12% smaller than our value. Previous measurements of the Hα/Hβ ratio with apertures large enough to include the whole nebula are O'Dell (1963), who obtained 4.2, and Peimbert & Torres-Peimbert (1971) who give 4.0; these agree well with our ratio of 4.05. Our *HST* results are not in good agreement with Rudy *et al.* (1991), who report Hα/Hβ = 4.55. Because of the uncertainty of the *HST* flux calibrations and possible contamination by scattered stellar light, for our discussion of the total and selective extinction, we adopt the ground-based values given in Table 3, and rescale our Hβ and Hα images appropriately.

Significant flux is seen in the halo in every emission line. The flux in the halo vs. the shell (including its interior) was measured by constructing a mask for each region. The halo mask extends to a radius of 6.″6. The boundary between the halo and shell was set at the contour line of Hβ=100 counts, which is about 9% of peak flux (Hβ=100 counts equals a pixel flux of Hβ=2.4×10^{-15} erg/s/cm^2). The flux from the central star was excluded by unmasking a circle centered on the star of radius $r=7$ pixels. The ratios of halo to shell flux are listed in Table 2. They range from 0.13 to 0.27. There is a trend for the fraction of scattered light to increase with decreasing wavelength as would be expected for scattering (see Fig. 3).

TABLE 3. Total fluxes and extinction.

	Observed[a]	Corrected for extinction by ISM[b]
Hβ	9.23×10^{-11}	1.26×10^{-10} erg s^{-1} cm^{-2}
Hα	3.76×10^{-10}	4.65×10^{-10} erg s^{-1} cm^{-2}
VLA	0.70	0.70 Jy [c]
$E_{\beta-\alpha}$	0.384	0.274
A_β	1.259	0.918
$R_{\alpha,\beta}$	3.28	3.35

[a]Hβ and Hα from: O'Dell (1963); O'Dell & Terzian (1970); Peimbert & Torres-Peimbert (1971).
[b]Using E_{B-V} = 0.093.
[c]VLA flux at 15 GHz.

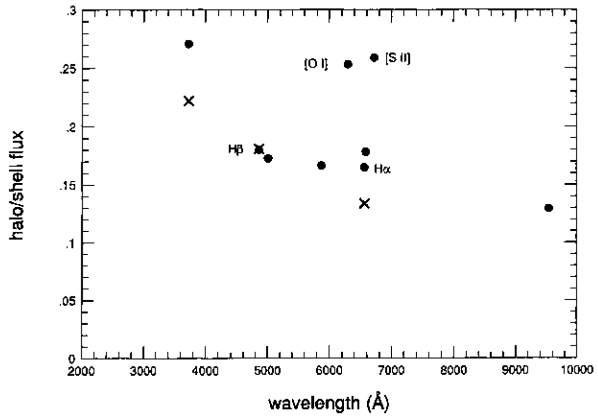

FIG. 3. The ratio of light in the halo to light in the shell as a function of wavelength. The crosses represent the Monte Carlo models discussed in Sec. 4.

There is an exponential decrease of line flux from the outer edge of the shell (i.e., the edge of the shell mask defined above) to the edge of the halo. The emission-line flux contours in the halo follow the elliptical shape of the shell. The radial profile of Hβ emission, measured from the outer edge of the shell, is smooth on a linear-log plot, and the profile is well fit by an exponential function except at small (close to the edge of the shell) and large (very low flux) radii (Fig. 4). To remove the elliptical shape of the shell and produce this radial plot, the image was converted to an angle-radius plot and each column (angle axis) was shifted to align the edge of the shell. Shifts ranged from 50–70 pix. The radial profiles in the other emission lines have the same exponential decrease; when scaled by their total halo flux relative to Hβ (Fig. 4), they are quite similar.

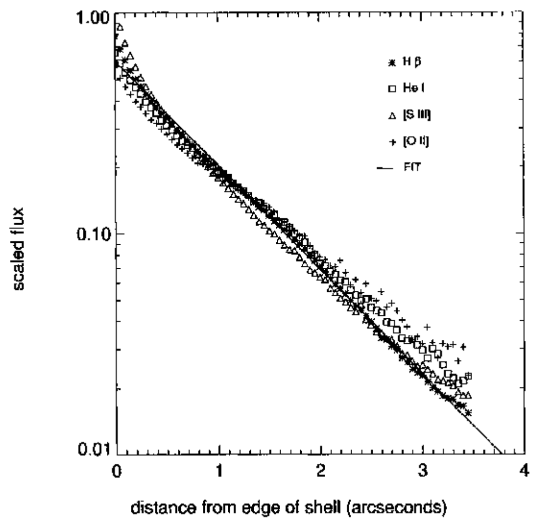

FIG. 4. The brightness of the halo as a function of distance from the edge of the shell as seen through four of the narrow band filters. The solid line is an empirical fit.

© American Astronomical Society • Provided by the NASA Astrophysics Data System

1997AJ....113.2147H

2.2 *VLA Radio Map and Radio Flux*

BD+30 is a bright radio source due to free–free emission from the ionized gas in the nebula. Radio images offer an absolute measure of the ionized gas content without any ambiguity due to extinction. In its widest configurations the Very Large Array[1] (VLA) can achieve a spatial resolution comparable to that of the *HST* images. We therefore obtained new high-resolution VLA data at 15 GHz in the VLA "A" configuration (4 hours on 1994 March 14), and combined them with earlier 5 and 15 GHz archival data (Masson 1989) from the less-extended "B" configuration which is more sensitive to large-scale features. Following standard calibration and self-calibration of the "B"-configuration data (the 15 GHz "A"-configuration data sample the very fine scale features and do not contain enough flux for self-calibration to succeed), the 5 and 15 GHz data from the two configurations were combined for mapping. This succeeds because the nebula is optically thin almost everywhere and thus the spectrum does not change significantly from 5 to 15 GHz (see discussion at the end of this section). Combining all the data provides an image in which the full range of spatial scales from 0".15 to 36" is fully sampled. The resulting uniformly-weighted image was deconvolved with a maximum entropy technique and restored with a Gaussian beam of 0".2.

Subsequently we rebinned the radio map to the same pixel scale as the *HST* images and aligned them by matching the small-scale structures. In Fig. 5 (Plate 44) we show the VLA image with the *HST* Hβ image for comparison. The rate of expansion of BD+30 has been measured from radio images to be 1.7 mas yr^{-1} (Masson 1989; Hajian *et al.* 1993; Kawamura & Masson 1996). In the 7.5 years between the two VLA observations used here the nebula expanded 13 mas, which is sufficiently smaller than the restoring beam used in the radio image (200 mas) that we can ignore it for present purposes.

As expected since both wavelengths arise from the same source, there is excellent morphological correspondence between the radio and Hβ images. All the filaments visible interior to the shell in the radio image, which are barely above the noise level, can be seen to have counterparts in the optical image, and bright radio knots in the shell have their optical counterparts. However, there is considerable variation in the relative brightness of features in the radio and optical images at different locations within the source, which we attribute to the effects of dust extinction. Prominent areas where this is apparent are the upper left corner of the shell and the whole western side of the shell, which are bright in the radio image but not in Hβ. The Hβ image also shows the effects of dust extinction in the light patches which dapple the shell, and of scattering in the halo which surrounds it. As can be seen in the lower-resolution images of Masson (1989), the radio images display a sharp outer boundary at the edge of the shell: no radio emission is found beyond the shell, where there is optical emission, down to a flux limit of approximately 10 mJy over a 10" square area.

[1]The Very Large Array is a facility of the National Radio Astronomy Observatory, which is operated by Associated Universities, Inc., under cooperative agreement with the National Science Foundation.

To avoid unsharp-masking effects in subsequent comparisons of the radio and optical data, the spatial resolution of the *HST* images must be degraded slightly to that of the VLA map (0".2). The Hβ and Hα images used in the ratio maps (e.g., Figs. 7 and 8) have been convolved with a 0".2 (4.4 pixel) Gaussian filter.

Bryce *et al.* (1997) recently reported high resolution radio observations of BD+30 obtained with the MERLIN array. The longer baseline 5 GHz MERLIN observations were combined with shorter baseline VLA data to generate a map of 0".08 resolution. They also show the ratio of this map with the *HST* Hβ image. It closely resembles our Fig. 7, not just in major features such as the dust blob and east-west gradient, but also in minor details such as the two parallel lanes running vertically down the west side of the shell.

In order to calculate reddening, an accurate value of the total radio flux is required for comparison with recombination line fluxes. Although the most accurate flux measurement available is from the 5 GHz data, these are affected by self-absorption. The peak 5 GHz brightness temperature in Fig. 5 is of order 3540 K, while the nebular temperature is 9000 K: this implies a peak optical depth of $\tau = 0.50$. The Bryce *et al.* MERLIN image has a higher resolution, and they find a peak brightness temperature of 5400 K at the same location, corresponding to an optical depth of $\tau = 0.92$. Such optical depths will significantly suppress the 5 GHz radio flux compared to its true optically thin value. However, at 15 GHz the optical depths are an order of magnitude lower than at 5 GHz, and self-absorption should be negligible.

We have therefore derived radio fluxes from the 1986 VLA "B"-configuration observation at 5 and 15 GHz separately. To do this we made images using natural weighting, which results in poorer spatial resolution but enhances sensitivity to any low-surface-brightness emission. We find fluxes of 0.64 ± 0.01 Jy at 4.87 GHz and 0.70 ± 0.02 Jy at 14.95 GHz (uncertainties are estimates only). These fluxes obtained from the images are compatible with an extrapolation of the corresponding visibility amplitudes to zero spacing (corresponding to a total flux), whereas other reported fluxes derived from these and other data tend to be too small to be compatible (e.g., Kawamura & Masson 1996 report 0.60 Jy at both 5 and 15 GHz). We assume that the difference between our fluxes and these values is that the latter were derived from images made so as to enhance spatial resolution (as was the case with our Fig. 5), and such images generally do a poorer job of including flux from any low-surface-brightness emission.

Assuming that we can neglect self-absorption in the 15 GHz flux, the frequency dependence of the Gaunt factor implies that the optically thin 5 GHz flux should be 0.80 Jy. The observed 5 GHz flux is 20% ± 5% below this value, corresponding to a mean optical depth of $\tau = 0.22$. If we assume a uniform temperature of 9000 K throughout the nebula, we can also estimate the effect of self-absorption directly from the radio image by applying a spatially varying correction of

$$f_\tau = \frac{T_e}{T_B} \ln\left(\frac{T_e}{T_e - T_B}\right) \quad (1)$$

© American Astronomical Society • Provided by the NASA Astrophysics Data System

1997AJ....113.2147H

to the image (Fig. 5). This results in an 8.4% increase in the flux, but we know this must be an underestimate since the MERLIN image indicates that our VLA image does not fully resolve all the structure in the nebula and the correction we derive will be too small in the small bright regions where this occurs. Further, in making Fig. 5 by combining 5 and 15 GHz data we assumed that the nebula is optically thin, and this will also not be correct in the brightest regions of the radio image. This assumption will further reduce the apparent brightness temperature of the brightest features and therefore also reduce the correction we derive in these locations. (Note that it will not affect the detailed morphology of the radio nebula.) Therefore we regard the 8% estimate derived from the image as an underestimate which is consistent with the estimate based on the comparison of 5 and 15 GHz fluxes, and in the following discussion we will use 0.70 Jy at 15 GHz for the optically thin radio flux of the nebula.

3. EXTINCTION AND REDDENING

3.1 Interstellar vs Intrinsic Reddening

Our *HST* images have clearly shown clumps of local absorbing material projected against the nebula (Arnaud *et al.* 1996), but since BD+30 lies only 5° above the galactic plane, we expect that some of the reddening will be interstellar. Pwa *et al.* (1986) observed UV interstellar absorption lines of S II and Zn II; these elements are not generally depleted in the ISM. Assuming a solar ISM abundance of S, they obtained a hydrogen column density of 5.5×10^{20} cm^{-2} from the S II λλ 1250,53,59 lines. Dinerstein & Sneden (1988) estimate an interstellar (H I + H_2) column from their observations of Na I absorption lines, and feel their results are consistent with the results of Pwa *et al.* (1986). From the relation $N_{\mathrm{H}}=5.9\times10^{21}$ E_{B-V} mag^{-1} cm^{-2} (Spitzer 1978), we see that this H column density should produce $E_{B-V}^{\mathrm{ISM}}\simeq0.093$ mag of selective extinction, which corresponds to $A_V^{\mathrm{ISM}}\simeq0.29$. Using the Seaton (1979) reddening curve, we find the corresponding extinction at Hβ to be $A_\beta^{\mathrm{ISM}}\simeq0.34$, the logarithmic extinction to be $c^{\mathrm{ISM}}\simeq0.136$, and the selective extinction between Hα and Hβ to be $E_{\beta-\alpha}^{\mathrm{ISM}}\simeq0.11$. As we will see below, these values are much smaller than the observed A_β or $E_{\beta-\alpha}$, which is consistent with the assumption that most of the extinction seen in BD+30 is intrinsic to the nebula itself. In the last column of Table 3 we list the observed total Hβ and Hα fluxes after correction for this presumed ISM extinction.

3.2 Selective Absorption: $E_{\beta-\alpha}$

The Hα/Hβ line ratio is frequently used to determine reddening for PNe. For BD+30, the integrated fluxes (Table 3) yield a mean value of Hα/Hβ=4.07 (3.69 after the ISM correction). Using the intrinsic Balmer decrement value of Hα/Hβ=2.86 (Case B, T=9000 K, $N_e=3.6\times10^4$ cm^{-3}; Hummer & Storey 1987), the selective extinction $E_{\beta-\alpha}$ is given by the formula

$$E_{\beta-\alpha}=2.5\ \log\frac{[\mathrm{H}\alpha/\mathrm{H}\beta]_{\mathrm{measured}}}{2.86}. \tag{2}$$

The integrated fluxes listed in Table 3 give a value of $E_{\beta-\alpha}=0.384$ (0.274 after the ISM correction). Adopting $f(\alpha)$-$f(\beta)$ =0.323 from the Seaton (1979) curve gives $c_{\mathrm{optical}}=0.475$. This is consistent with the value of $c=0.46$ found by LeVan & Rudy (1983), but significantly smaller than other published values ($c=0.65$: Kaler 1976; Rudy *et al.* 1991).

Figure 6 (Plate 45) shows the map of $E_{\beta-\alpha}$ after correction for interstellar reddening. We see that there are significant variations in $E_{\beta-\alpha}$ across the nebula. In the north-east where the dust blob is superimposed on the shell, $E_{\beta-\alpha}\sim0.9$. Typical values in the rest of the shell are $E_{\beta-\alpha}\simeq0.4-0.5$. Variation within the shell is small, with $E_{\beta-\alpha}$ somewhat larger on the right side (west) and with a tendency to decrease as the radius decreases, to ratios of about 0.25–0.35. In this map, the shell appears thinner on the left side, contributing to its lower average value. Just outside the shell, the ratio appears to drop to $E_{\beta-\alpha}\simeq0.1$, then increases in the halo to about $E_{\beta-\alpha}\simeq0.3$ again (however, the fluxes are low in the halo and the ratio map shows a lot of noise there).

3.3 Total Absorption: A_β

Comparison of the Hβ flux with the radio flux should yield the total absorption. The number of Hβ photons produced relative to the radio emission is dependent on the temperature (9000 K), electron density (3.6×10^4 cm^{-3}), Gaunt factor and atomic constants, and the $N(\mathrm{He}^+)/N(\mathrm{H}^+)$ ratio. Most of the helium is neutral in BD+30; we find $N(\mathrm{He}^+)/N(\mathrm{H}^+)=0.023$ from the strength of He I λ5876. We obtain S_ν(Jy)/Hβ(erg)=2.38×10^9 at ν = 14.94 GHz. Thus the total extinction at Hβ is given by the formula:

$$A_\beta=2.5\ \log\frac{[\mathrm{VLA}]_{15\ \mathrm{GHz}}/[\mathrm{H}\beta]_{\mathrm{measured}}}{2.38\times10^9}. \tag{3}$$

The integrated fluxes give $A_\beta=1.26$ (0.92 after the ISM correction). Since $A_\beta=2.5c$, the total logarithmic extinction is $c_{\mathrm{radio}}=0.50$. The full map of A_β (corrected for interstellar extinction: Fig. 7, Plate 46) shows values on the right (west) side of the shell to be higher than those on the left ($A_\beta\sim1.5$ vs $A_\beta\sim0.8$). The A_β map looks qualitatively similar to the $E_{\beta-\alpha}$ map, although the halo is not present in the A_β map, since the radio emission ends abruptly at the edge of the bright shell. In the north-east dust blob, A_β reaches 2.5 – 3. Although the central core shows a few wisps of very low extinction, this may be an artifact of the scarcity of radio emission in the core combined with dust-scattered Hβ flux.

4. A_V/E_{B-V} AND THE NATURE OF THE DUST IN BD+30

The ratio of total to selective reddening, $R=A_V/E_{B-V}$, is a quantity of considerable interest. From the Hβ, Hα, and radio fluxes we can derive a related quantity, $R_{\alpha,\beta}$ = $A_\beta/E_{\beta-\alpha}$. From the values in the preceding section, we obtain $R_{\alpha,\beta}$ = 3.28. If we use the values after correction for the presumed ISM extinction, the result is $R_{\alpha,\beta}$ = 3.35. These

© American Astronomical Society • Provided by the NASA Astrophysics Data System

1997AJ....113.2147H

values are similar to that found for the interstellar medium, where the Seaton (1979) extinction curve leads to $R_{\alpha,\beta}$ = 3.0.

Although $R_{\alpha,\beta}$ is qualitatively the same as R (and has a similar numerical value for the standard ISM extinction curve), we cannot derive one from the other without introducing assumptions about the shape of the extinction curve. Under the assumption that the shape of the curve throughout the visible remains invariant, while a variable amount of neutral extinction is present, Miller & Mathews (1972) showed that the value of R based on the Whitford (1958) curve is given by

$$R=\frac{A_\beta-0.425E_{\beta-\alpha}}{0.863E_{\beta-\alpha}}=1.16R_{\alpha,\beta}-0.492. \tag{4}$$

We use instead the Seaton (1979) curve to obtain $R=1.25R_{\alpha,\beta}-0.494$. Our value of $R_{\alpha,\beta}$ = 3.28 for BD+30 then yields $R=3.6$, not much larger than the standard ISM value of 3.1.

In Fig. 8 (Plate 47) we show a map of $R_{\alpha,\beta}$ after removal of the presumed ISM extinction. We see that $R_{\alpha,\beta}$ is higher on the right (west) side (which is also the side with the highest extinction). There is small scale variation seen throughout shell of the nebula. We display $R_{\alpha,\beta}$ because in cases where there are absorbing layers between the observer and an extended source of radiation, this quantity should be constant even if there are large variations in the optical depth to different points on the object. On the other hand, if dust is mixed with the emitting material, the value of $R_{\alpha,\beta}$ will increase with the optical depth. [See Appendix A, Eqs. (A9) and (A12).] The first situation seems to fit the behavior of the north-east dust blob, where, although it is the strongest feature on both the $E_{\beta-\alpha}$ and A_β maps, it practically disappears in $R_{\alpha,\beta}$. The general east-west gradient is probably related to the second effect, i.e., dust within the emitting shell with greater optical depths in the west. Scattering adds to the complexity, however. For example, consider what happens to $R_{\alpha,\beta}$ if we have a line of sight where there is little emitting gas, so that scattered Hα and Hβ is dominant—there will be little radio flux from this region and thus A_β could be very small or even become negative.

Most of our information about the dust in BD +30°3639 stems from the numerous infrared observations (e.g., Moseley & Silverberg 1985). There is no evidence of silicate features at 9.7 or 18 μm, so it is believed that the main constituent of the grains is carbon. There is an 11.2 μm feature attributed to SiC. Hoare *et al.* (1992) modeled the far infrared emission and concluded that dust must be present in both the ionized shell and in the neutral halo, where the dust would be cool and would thus provide the far infrared excess not explained by the hotter dust in the ionized gas. They also concluded that amorphous carbon was a more satisfactory grain material than graphite, and that there is about 1/10 as much SiC as carbon. A model was also produced by Siebenmorgen *et al.* (1994), who added small grains to fit the near infrared. Our observations relate to a different facet of the dust, namely, the optical extinction and scattering properties.

We would like to use A_λ and $R_{\alpha,\beta}$ to infer the physical properties of the dust. The relevant equations are given in Appendix A. If the model of a layer of extinction between the nebula and the observer were applicable here, then from Eq. (A9) the observed $R_{\alpha,\beta}=3.35$ would imply that $\bar{Q}_{\rm ex}(\lambda_\beta)=1.43\bar{Q}_{\rm ex}(\lambda_\alpha)$. For amorphous carbon, we adopt the optical constants derived by Rouleau & Martin (1991) from laboratory measurements of benzene burned in air (sample "BE1"). Using Mie theory with these constants to evaluate $\bar{Q}_{\rm ex}(\lambda)$ as defined by Eq. (A4), we find that for the MRN distribution (Mathis *et al.* 1977: $a_-=0.005$, $a_+=0.25$, $\gamma=0.5$) $\bar{Q}_{\rm ex}(\lambda_\beta)=1.29\bar{Q}_{\rm ex}(\lambda_\alpha)$. If we use a (probably more realistic) grain size distribution with an exponential roll-off for large grains, taking $a_-=0.001$, $a_b=0.10$, and $\gamma=0.2$, we find $\bar{Q}_{\rm ex}(\lambda_\beta)=1.40\bar{Q}_{\rm ex}(\lambda_\alpha)$, equivalent to $R_{\alpha,\beta}=3.5$.

The actual situation is more complicated, since we are dealing with dust mixed with the emitting gas, surrounded by a neutral, dusty halo. We have considered spherical models which consist of a hollow shell of emitting gas with a thickness 1/6 its radius, surrounded by a scattering/absorbing halo twice the radius of the emitting shell. The dust is supposed to be present in the emitting gas as well. For all these models, we adopt the grain size distribution (A6) with $a_-=0.001$, $a_b=0.10$, and $\gamma=0.2$. Using amorphous carbon as above, we find that the albedo of this distribution is $\bar{Q}_{\rm sc}(\lambda_\beta)/\bar{Q}_{\rm ex}(\lambda_\beta)=0.255$. Using the Mie theory phase function and solving the transfer problem by Monte Carlo methods as described in Appendix B, we find that for a model with a radial optical depth $\tau_0(\lambda_\beta)=0.83$, 34% of the photons escape directly, 9% escape after scattering, and 57% are absorbed, which is equivalent to an extinction at Hβ of $A_\beta=0.92$, as observed. The wavelength dependence of the amorphous carbon dust distribution would then imply $\tau_0(\lambda_\alpha)=0.594$. Solving the corresponding scattering problem for this optical depth (the albedo is 0.261 at λ_α), we find that 46% escape directly, 9% escape after scattering, and 45% are absorbed, leading to $A_\alpha=0.65$. Thus the more sophisticated treatment of the radiative transfer problem has improved the fit slightly, reducing $R_{\alpha,\beta}$ from 3.5 for the extinction layer model to 3.4, closer to the observed $R_{\alpha,\beta}=3.35$.

The difficulty with this model is the surprisingly large fraction of light from the emission lines which appears to be scattered from dust in the halo outside the ionized shell. If we examine the distribution of scattered Hβ photons in the model, we find that of the 8.9% of the light which is scattered out of the nebula by dust, only 3.72% appears as a halo, while 5.18% of it is projected on the ionized shell and adds to its apparent brightness. Thus the halo/shell flux ratio of the model would be 0.0955, about half the observed value of 0.18.

For a given optical depth, we can increase the fraction of scattered light which the observer sees as a halo by increasing the radius of the halo relative to the emitting shell. We reject this approach because the decline in halo brightness with radius then becomes too flat to fit our observations. Another possibility is that a spherical model is not a good approximation. Indeed, there are some indications that the nebula is elongated along our line of sight (Masson 1989). Because the dust is strongly forward scattering, this may lead

© American Astronomical Society • Provided by the NASA Astrophysics Data System

1997AJ....113.2147H

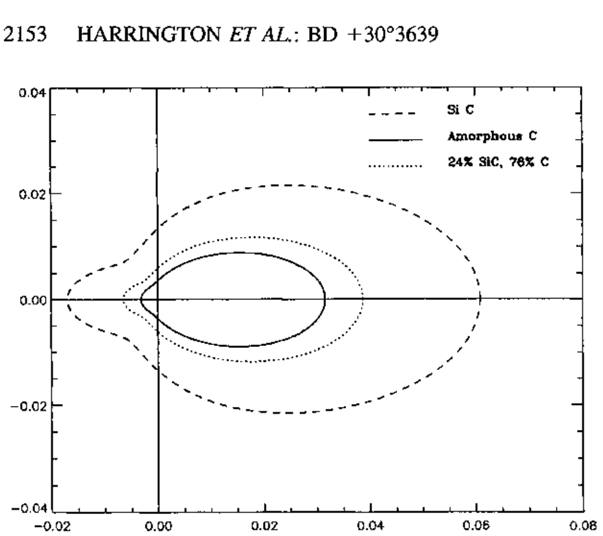

FIG. 9. The scattering phase function of particle distributions for SiC, amorphous carbon, and a mixture of the two at $\lambda_\beta = 0.4861\mu$m. The number of particles as a function of radius is given by Eq. (A6), with $a_- = 0.001$, $a_b = 0.10$, and $\gamma = 0.2$. The horizontal axis to the right is forward scattering. The integral over 4π steradians gives the total effective scattering cross section $\bar{Q}_{sc}(\lambda_\beta)$.

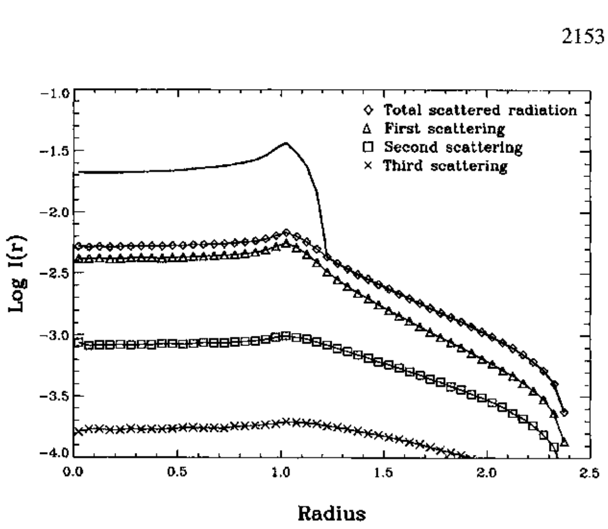

FIG. 10. Results of the Monte Carlo calculation described in the text. The solid line represents the total intensity, direct plus scattered. The edge of the emitting shell is at radius 1.2, while the scattering halo ends at 2.4 (arbitrary units). The radial optical depth of the model from the center to the edge of the halo is $\tau_0(\lambda_\beta) = 0.98$.

to increased halo brightness, though detailed computations are needed to quantify such an effect.

Here, we consider the possibility that the dust albedo is higher than that given by the adopted carbon grain model. In particular, the nebular dust is known to contain silicon carbide, which is refractive at optical wavelengths, and hence would have an albedo near unity. Our Monte Carlo models show that we can match the observed halo/shell ratio if we raise the albedo to 0.40. If we consider a mixture of 76% amorphous carbon and 24% SiC, the albedo of the mixture will be 0.40 for our adopted grain size distribution. The scattering phase functions of the two components and of the mixture are shown in Fig. 9. Because of the increased scattering, we must set $\tau_0(\lambda_\beta) = 0.98$ to obtain the observed extinction of $A_\beta = 0.92$. In the resultant model, 28% of the photons escape directly, while 14.8% escape after scattering. Of these, 8.2% are projected on the shell and 6.6% appear as a halo. The resultant halo/shell ratio is 0.181.

In Fig. 10 we show the radial intensity distribution of the model. The solid curve is the sum of direct and scattered light, while the diamonds represent the escaping scattered light. Note that the emitting shell is between 1.0 and 1.2, while the halo extends from 1.2 to 2.4. The triangles represent light escaping after one scattering, squares that which is scattered twice, and crosses the third scattering.

In Fig. 11 we compare the scattered light distribution in this model with one in which the scattering is isotropic. For isotropic scattering, the far halo is brighter, while the near halo and especially the interior are fainter. The total halo/shell ratio is 0.185 for the isotropic scattering model.

In addition to the total halo flux, we have information on the brightness distribution. Figure 12 compares the radial intensity distribution with the observed brightness profile. There is good agreement in the slope of the halo intensity. The observed halo extends beyond the halo in our model, but as noted earlier, if we make our (constant density) halo larger, the model profile flattens and no longer fits the observed slope. It is likely that the halo is in fact larger, but with decreasing density, which could preserve the steep slope.

Having constructed a model which reproduces the basic features of the halo seen through the Hβ filter, it is of interest to examine the implications for other wavelengths. The optical depth of our SiC-C mixture model at the wavelength of Hα is 0.685 and the albedo is 0.391. The resulting halo/shell ratio at Hα is 0.134, which may be compared to the observed 0.165. The extinction $A_\alpha = 0.64$ for this model, almost identical to the pure amorphous carbon model discussed above. The optical depth at λ3727 for our dust model is 1.267 and the albedo is 0.408. With these parameters, the Monte Carlo model gives a halo/shell ratio of 0.222. These results are plotted with the observed values on Fig. 3. We see that the models reproduce the general increase of halo brightness toward shorter wavelengths, but do not give detailed agreement.

Finally, these models help us interpret the ratio maps of

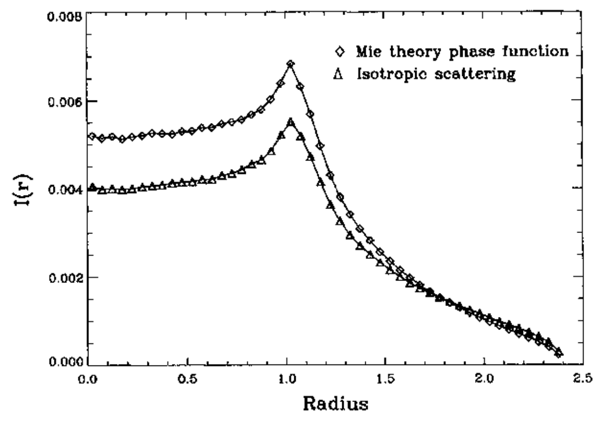

FIG. 11. Comparison of the total scattered light from a model with isotropic scattering compared to the model using the mixture phase function shown in Fig. 9.

© American Astronomical Society • Provided by the NASA Astrophysics Data System

1997AJ....113.2147H

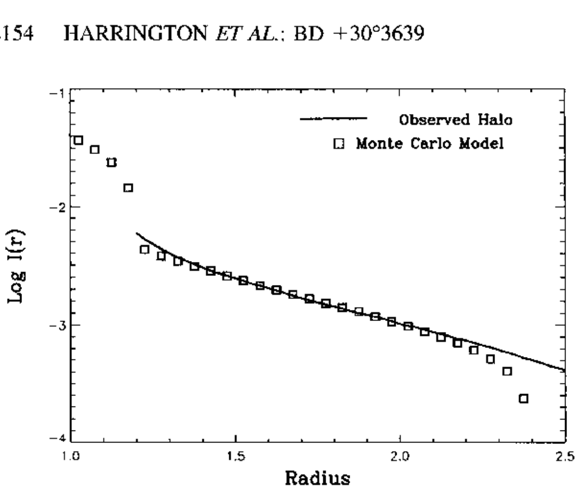

FIG. 12. The observed mean Hβ halo intensity compared to the Monte Carlo model of Fig. 10. The zero point has been adjusted for the best fit—we are only interested in the slope of the brightness curve.

this nebula. Figure 13 shows the Hβ/Hα ratio from our Monte Carlo models. We see that the halo is bright since it is entirely scattered light, and the scattering is greater at Hβ. The bright rim of the emitting shell, on the other hand, is a minimum in the ratio image, since this feature is primarily due to directly escaping radiation, and the higher extinction at Hβ is dominant. In the interior of the shell, the scattered radiation competes with the direct radiation to give an intermediate intensity. Disregarding the large absorption blob in the real nebula, the overall appearance of the observed Hβ/Hα ratio image shows just these features.

5. EMISSION FEATURES IN THE HALO

Ratio maps are useful in detecting not only ionization stratification effects in the ionized shell but also features in the halo. Except for the intrusion of the NE dust blob into the halo, the Hα/Hβ ratio is smooth there (see Fig. 6). In Fig. 14 (Plate 48) we show a number of ratio maps, made with the Balmer line closest in wavelength. This will reduce any effects due to changes in the scattering cross-section with wavelength. Ratio maps of [O III]/Hβ and He I/Hβ show

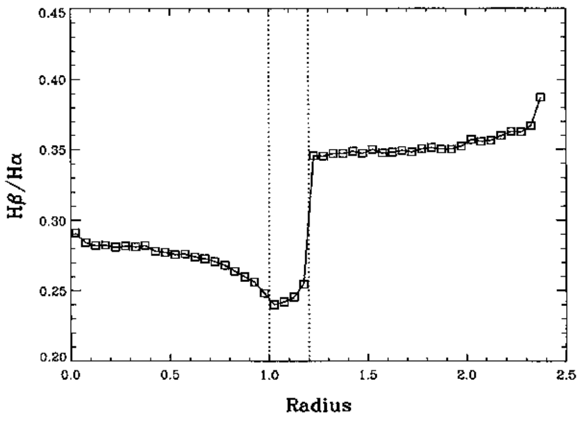

FIG. 13. The ratio of the total light from the Hβ and Hα Monte Carlo models, as discussed in Sec. *4.1*. The dotted lines show the location of the emitting shell in the models.

clear ionization stratification: the ratio is high at the inner edge of the shell, but drops strongly in the outer ionized shell where the ionization level has dropped. The ratio rises again in the halo as scattered light replaces direct emission. The inverse effect is seen in the low ionization lines, [N II]/Hα and [O I]/Hα, where the edge of the shell is marked by an increase in the ratio. (In these maps, a mask based on the strength of the Hβ line limits the region displayed; as a result ratios involving lines with relatively less signal, such as [O III] and [O II], appear rather noisy.)

Perhaps most interesting are the ratio maps made from the two lines with the highest halo/shell ratios, [S II]/Hα and [O I]/Hα. These maps show prominent structures in the halo—which we would not expect from a ratio of scattered light, since the fraction scattered should change little over a few hundred Å. Structures to be noted include an east blob with some fluff, an east filament that curls around the large NE dust blob, western fluff, and some southern radial spokes. The structures are not the same in the [S II] and [O I] images, except for the east blob. The position of this feature coincides with extended emission seen in the 1–0 $S(1)$ transition of H_2 (Graham *et al.* 1993).

Because the halo structures seen in [S II]/Hα and [O I]/Hα are not apparent in the other lines or in ratios such as Hβ/Hα or [O II]/Hα, it is hard to see how they can be due to scattered light. Outside the ionized shell, oxygen will be neutral, but elements with ionization potentials below hydrogen, such as carbon, silicon, sulfur, etc. may be singly ionized. However, to produce optical emission, we need some mechanism to heat the neutral halo gas to $\sim$5000 K.

We may first examine gas heating by far-UV photons with energies less than 13.6 eV. While this explanation seems attractive, detailed photodissociation models fail to account for the observed strength of [O I] and [S II] emission. For example, with the H_2 2.12 μm flux of 3.5×10^{-13} ergs cm^{-2} s^{-1}, measured through a 10″ aperture centered on the star (Beckwith *et al.* 1978), the [S II] $\lambda\lambda$ 6717, 6731/ H_2 2.12 μm flux ratio in the western feature must be larger than 0.06. This large flux ratio is characteristic of very dense ($n \geq 10^6$ cm^{-3}) photodissociation regions produced by strong far-UV radiation fields (Hollenbach & Natta 1995), much denser than the BD+30 photodissociation region. Time-dependent photodissociation models of BD+30 (Hollenbach & Natta 1995) produce negligible amounts of [O I] and [S II] emission. While H_2 emission in BD+30 might be produced by fluorescence alone (Shupe *et al.* 1997), the [O I] and [S II] emission excess seems to require some other source of heating.

Another possibility to be considered is the heating which might be produced by penetration of high-energy photons, especially since BD+30 is an X-ray source. To estimate this effect quantitatively, we extended a photoionization model of BD+30 made earlier with Harrington's code (Ferland *et al.* 1995) to include the neutral shell, using Ferland's CLOUDY. Models were made with two radiation fields, the first of which was a $3900L_\odot$ star represented by a 35,000 K model atmosphere. For the second case, we added a bremsstrahlung component with a temperature of 3×10^6 K. The intensity of this component was chosen to

© American Astronomical Society • Provided by the NASA Astrophysics Data System

1997AJ....113.2147H

provide an integrated flux at the earth of 0.9×10^{-12} ergs cm^{-2} s^{-1} between 0.4 and 1.8 keV, as observed (Arnaud *et al.* 1996). Both models fit the observed nebular optical fluxes well, and are nearly indistinguishable in the ionized zone. In the first model, the temperature in the neutral gas drops immediately to $\sim$250 K and declines slowly. In the model with the X-rays, the temperature in the neutral gas drops to $\sim$600 K, again declining slowly to below $\sim$300 K. The hydrogen in the models becomes molecular about 2/3 of the way through the neutral shell. In neither model is there sufficient heating in the atomic hydrogen zone to produce any optical emission.

Finally, we consider the possibility that the [O I] and [S II] emission could be produced by shocks propagating through the halo with velocities sufficient to heat the gas but not ionize it. To make a quantative estimate, let us consider a shock of velocity $u_0=15$ km/s. Since the mean molecular weight of the neutral gas will be $\mu\sim1.3$, the temperature behind the shock will be $T=6600$ K. (We choose this shock velocity solely to produce the minimum temperature needed for effective collisional excitation of O^0 and S^+.) Consider a spherical shock front of radius R propagating into a halo of density n_0. Then the rate at which the shock adds kinetic energy to the halo gas will be

$$L_{shk}=\tfrac{3}{2}kT\ n_0u_0 4\pi R^2\frac{\Omega}{4\pi}, \qquad (5)$$

where we suppose the shock only subtends a solid angle Ω as seen from the star. To the extent that this shock is radiative and has reached a steady state, this energy will be radiated away in the region behind the shock. If the radius R subtends an angle ϕ at the distance D of the nebula, then the flux we observe will be

$$F_{shk}=\frac{L_{shk}}{4\pi D^2}=\tfrac{3}{2}kT\ n_0u_0\phi^2\frac{\Omega}{4\pi}. \qquad (6)$$

We have attempted to estimate the emission in excess of the scattered background in the [O I] and [S II] features. Thus the excess [S II] emission in the feature in the western halo is 2×10^{-14} erg cm^{-2} s^{-1}. If we take the shock parameters above, with $\phi\sim5''$ and $\Omega\sim0.2$, we find that we require $n_0\sim10^3$ cm^{-3} if all the energy is radiated away in this line. While such efficiency is not realistic, this density is over an order of magnitude lower than that in the ionized shell. Thus it seems reasonable that shocks driven into a halo with densities comparable to those in the ionized shell could explain the observed [O I] and [S II] emission.

6. CONCLUSIONS

We have compared a high-resolution VLA radio continuum map of BD+30 with nine *HST* narrow-band filter images. We find evidence for dust both mixed with the ionized gas (the gradient in the $R_{\alpha,\beta}$) and external to the ionized zone (the scattered light halo; the blob present in the $E_{\beta-\alpha}$ map but not in $R_{\alpha,\beta}$). The average value of R for this dust seems to be near 3, similar to the ISM value, and can be modeled by a power law distribution of amorphous carbon grains.

The optical images all display halos of light outside the ionized shell delineated by the radio image. The characteristics of these halos indicate that they are due to light from the ionized gas which is scattered in the (previously known) neutral gas outside the ionized zone. We have measured the fraction of light in the halos and the average brightness as a function of radius. The fraction of light in the halo may exceed 20% of the total. We have constructed radiative transfer models and find that the halos can be explained if the dust in the halo has an optical depth around unity and an albedo of $\sim$0.4. However, the published optical constants of amorphous carbon, the most likely grain material, when used with a realistic distribution of particle sizes, yield a much smaller albedo. We suggest that either some other grain material with a high albedo, such as SiC, makes an important contribution to the dust, or that the carbon in the nebula has a higher albedo than that implied by the optical constants derived from laboratory measurements of the products of benzene combustion which we have used.

We find that ratio maps show structures in the halo which are not otherwise apparent. While some ratio maps are quite smooth, [O I]/Hα and [S II]/Hα show various features, the most prominent of which is coincident with a known peak of H_2 emission. We suggest that since the oxygen and sulfur in the halo will be in the form of O^0 and S^+, these features may be due to emission produced by shocks propagating through the neutral halo.

Finally, we note that comparison of the 6 cm and 2 cm radio fluxes indicates a substantial free-free absorption in the nebula at 6 cm. This absorption is more than we would infer from the brightness temperature of our radio map, and thus indicates unresolved high-density fine structure. Bryce *et al.* (1997) obtained densities as high as 5×10^5 cm^{-3}, but this result depends upon the rather low electron temperature of 5690 K derived by Basart & Daub (1987) from the radio spectrum. But even if the forbidden line temperature of $\sim$9000 K is adopted, there still must be high density regions. We note that Arnaud *et al.* (1996) found that the pressure of the X-ray emitting gas and of the stellar wind seemed higher than could be supported by the assumed density of $\sim4\times10^4$ cm^{-3}. It may be that an increasing stellar wind pressure has initiated a series of effects, including the formation of dense structures in the ionized shell, shocks driven into the neutral halo, and the high-velocity outflow in CO (±50 km s^{-1}) seen by Bachiller *et al.* (1991) and in H_2 by Shupe *et al.* (1997). We note that molecular gas in BD+30, as seen through its CO and H_2 emission, is associated with this bipolar outflow and not with the neutral dusty halo revealed by the *HST* images.

We thank Colin Masson and Barry Clark for permitting the use of VLA archival data in this project. Thanks also to Myfanwy Bryce for providing a preprint of Bryce *et al.* (1997). Support for this work was provided by grants GO-5403.01-93A and GO-5404.01-93A from the Space Telescope Science Institute, which is operated by the Association of Universities, Inc., under NASA contract NAS5-26555.

© American Astronomical Society • Provided by the NASA Astrophysics Data System

1997AJ....113.2147H

APPENDIX A. DUST EQUATIONS

If an object with intensity $I(\lambda)$ would have an intensity $I_0(\lambda)$ in the absence of extinction, then the extinction in magnitudes, A_λ, is related to the optical depth of the dust, $\tau(\lambda)$, by

$$A_\lambda = 2.5 \log_{10}\left(\frac{I_0(\lambda)}{I(\lambda)}\right) = 2.5 \log_{10} e^{\tau(\lambda)} = 1.0857\tau(\lambda). \tag{A1}$$

In the case of interstellar extinction, where the star or nebula is at some distance D, the optical depth is

$$\tau(\lambda) = \int_0^D \kappa(\lambda,r)dr. \tag{A2}$$

If the dust consisted of spherical grains of radius a, we could express $\kappa(\lambda,r)$ as

$$\kappa(\lambda,r) = n_d(r)\pi a^2 Q_{\rm ex}(\lambda,a) = \frac{3m_H\mathfrak{R}}{4\rho a} n_{\rm H}(r) Q_{\rm ex}(\lambda,a). \tag{A3}$$

Here, $n_d(r)$ is the number of grains cm^{-3} and $Q_{\rm ex}(\lambda,a)$ is the dimensionless extinction efficiency factor. If we define $\mathfrak{R}$ as the dust to hydrogen ratio by mass and ρ as the density of the grain material, the right hand side expresses $\kappa(\lambda,r)$ in terms of the hydrogen density $n_{\rm H}(r)$. The extinction is the sum of two terms, the absorption and the scattering, so that $Q_{\rm ex}(\lambda,a) = Q_{\rm ab}(\lambda,a) + Q_{\rm sc}(\lambda,a)$.

More realistic models of interstellar extinction consider a distribution of grain sizes, often assumed to follow a power law distribution. Thus, if the number of grains of radius a is $N_d(a) \propto a^{-(3+\gamma)}$ (i.e., $m(a) \propto a^{-\gamma}$) for a range of radii $a_- \leq a \leq a_+$, then Eq. (A3) is still valid if we replace $Q_{\rm ex}(\lambda,a)$ by a mean efficiency factor $\bar{Q}_{\rm ex}$ defined as

$$\bar{Q}_{\rm ex}(\lambda) = \frac{\gamma}{a_-^{-\gamma} - a_+^{-\gamma}} \int_{a_-}^{a_+} a^{-(\gamma+1)} Q_{\rm ex}(\lambda,a) da \tag{A4}$$

and substitute for a a mean grain radius $\bar{a}$ defined by

$$\bar{a} = \frac{\gamma}{1-\gamma}\left(\frac{a_+^{1-\gamma} - a_-^{1-\gamma}}{a_-^{-\gamma} - a_+^{-\gamma}}\right). \tag{A5}$$

While the shape of the extinction curve is not too sensitive to the maximum grain size a_+, the large grains are important for the albedo and the scattering phase function. Since an abrupt cut off at some maximum grain radius a_+ seems unphysical, a more reasonable model might be one in which the number of large grains declines exponentially above some value a_b; such an expression has been used by, e.g., Kim & Martin (1996), who consider a mass distribution of the form $m(a) \propto a^{-\gamma}\exp(-a/a_b)$, equivalent to the size distribution

$$N_d(a) \propto \exp(-a/a_b) a^{-(3+\gamma)}, \quad \text{for } a_- \leq a < \infty. \tag{A6}$$

Let us now define the mean efficiency factor $\bar{Q}_{\rm ex}$ as

$$\bar{Q}_{\rm ex}(\lambda) = \frac{1}{\Gamma(-\gamma,x_0)} \int_{x_0}^{\infty} x^{-(\gamma+1)} e^{-x} Q_{\rm ex}(\lambda,a) dx, \tag{A7}$$

where $x = a/a_b$, $x_0 = a_-/a_b$, and $\Gamma(-\gamma,x_0)$ is the incomplete gamma function. If we further define the mean radius $\bar{a}$ as

$$\bar{a} = \frac{\Gamma(1-\gamma,x_0)}{\Gamma(-\gamma,x_0)} a_b, \tag{A8}$$

then once again the dust opacity is given by Eq. (A3).

It follows from Eqs. (A1), (A3) and the definition of $R_{\alpha,\beta}$ that

$$R_{\alpha,\beta} = \frac{A_\beta}{A_\beta - A_\alpha} = \frac{1}{1-\epsilon}, \tag{A9}$$

where $\epsilon = \bar{Q}_{\rm ex}(\lambda_\alpha)/\bar{Q}_{\rm ex}(\lambda_\beta)$ and $\lambda_\alpha = 0.6563$ μm and $\lambda_\beta = 0.4861$ μm, the wavelengths of Hα and Hβ. Thus $R_{\alpha,\beta}$ is constant for a given reddening curve.

The situation is more complicated if dust is mixed with the emitting gas. In this case, neglecting scattering, the intensity is given by an expression of the form

$$I(\lambda) = \int_0^\infty e^{-\tau(\lambda,r)} j(\lambda,r) dr. \tag{A10}$$

Consider the simple model where the ratio of line emission to dust extinction, $j(\lambda,r)/\kappa(\lambda,r)$, is constant. In this case $I(\lambda)/I_0(\lambda) = (1 - e^{-\tau_0(\lambda)})/\tau_0(\lambda)$, where $\tau_0(\lambda)$ is the total optical depth of the nebula. It follows that the extinction in magnitudes is given by

$$A_\lambda = 2.5 \log_{10}\left(\frac{\tau_0(\lambda)}{1 - e^{-\tau_0(\lambda)}}\right), \tag{A11}$$

and is therefore no longer linear in $\bar{Q}_{\rm ex}(\lambda)$. The expression for $R_{\alpha,\beta}$ then becomes

$$R_{\alpha,\beta} = \left[\log_{10}\frac{\tau}{1-e^{-\tau}}\right]\left[\log_{10}\frac{1-e^{-\epsilon\tau}}{\epsilon(1-e^{-\tau})}\right]^{-1}. \tag{A12}$$

Here τ represents $\tau(\lambda_\beta)$. This expression reduces to (A9) in the limit $\tau \rightarrow 0$, but is otherwise larger. Thus, for the Seaton (1979) reddening curve, $\epsilon = 0.677$, and values of $R_{\alpha,\beta}$ for τ = 0, 0.5, 1, 2, 3, and 5 are 3.08, 3.19, 3.29, 3.54, 3.82, and 4.45.

In reality, the presence of the halo indicates that scattering is important, i.e., the emissivity $j(\lambda,r)$ contains an integral over the radiation field. Because the scattering is not isotropic, and because the optical depth is of the order of unity, which implies that multiple scattering cannot be neglected, we have resorted to Monte Carlo models, which are described in Appendix B.

APPENDIX B. MONTE CARLO SCATTERING MODELS

We considered models with dust composed of amorphous carbon, as well as a mixture of carbon and silicon carbide. The amorphous carbon optical constants were taken from Rouleau & Martin (1991), while those for SiC were from Choyke & Palik (1985). We computed the angular scattering phase functions from Mie theory using the methods of Barber & Hill (1990). The phase function was calculated for 300 values of the particle radius and averaged over the size distribution (A6) discussed in Appendix A. Because amorphous

© American Astronomical Society • Provided by the NASA Astrophysics Data System

1997AJ....113.2147H

carbon is highly absorbing, the albedo of small particles is very low and it is only the larger particles, which tend to be forward-scattering, that contribute to $\bar{Q}_{sc}(\lambda)$. In the case of SiC, which is refractive at optical wavelengths, there is more side and back scattering. We adopted a particle distribution with $a_- = 0.001$, $a_b = 0.10$, and $\gamma = 0.2$; this distribution of carbon particles gives a wavelength variation of optical extinction similar to the standard ISM curve. The averaged phase functions which result are shown in Fig. 9.

We consider the simplest geometry which still captures the essential features of the nebula: a spherical dust shell of radius R surrounding a hollow cavity of radius unity. The line emission is assumed to arise from a homogeneous inner part of the shell, $1<r<1+S$, while it is assumed that there is no emission in the neutral halo, $1+S<r<R$. The dust opacity is taken to be uniform in both the ionized and neutral gas, $1<r<R$. The results presented here are for the case $S=0.2$ and $R=2.4$, i.e., the halo is twice the outer radius of the thin ionized shell.

Routines were written in "J" (an APL dialect) to follow groups of 2×10^4 photons emitted in random directions from points $1<z<1+S$ on the z-axis, until they were either absorbed or escaped the halo. Actually, to improve the statistics of the higher order scatterings, photons were always scattered and followed through the fourth scattering or until exit. Subsequently, the number of photons escaping after the nth scattering were reduced by the nth power of the albedo. This method has the additional advantage of providing the solution for all values of the albedo without recalculation. The impact parameters of the exiting photons were saved and binned in 48 radial intervals. The number in each bin divided by the mean radius of that bin is then the radial intensity distribution seen by an external observer. About 10^7 photons were followed per run. For the albedos and optical depths considered here, the number of photons which had not escaped or been absorbed by the fourth scattering was negligible compared to the statistical errors of the sample. Since the radiation field becomes partially polarized after the first scattering, one should actually carry the polarization and use separate scattering cross-sections for the two polarizations, but this effect was neglected.

REFERENCES

Arnaud, K., Borkowski, K. J., & Harrington, J. P. 1996, ApJ, 462, L75

Bachiller, R., Huggins, P. J., Cox, P., & Forveille, T. 1991, A&A, 247, 525

Balick, B. 1987, AJ, 94, 671

Balick, B., Gonzalez, G., Frank, A., & Jacoby, G. 1992, ApJ, 392, 582

Barber, P. W., & Hill, S. C. 1990, Light Scattering by Particles: Computational Methods (World Scientific, Singapore)

Basart, J. P., & Daub, C. T. 1987, ApJ, 317, 412

Beckwith, S., Persson, S. E., & Gatley, I. 1978, ApJ, 219, L33

Bryce, M., Pedlar, A., Muxlow, T., Tomasson, P., & Mellema, G. 1997, MNRAS, 284, 815

Campbell, W. W. 1894, A&A, 13, 461

Choyke, W. J., & Palik, E. D. 1985, in Handbook of Optical Constants of Solids, edited by E. D. Palik (Academic, Boston), p. 587

Dinerstein, H. L., & Sneden, C. 1988, ApJ, 335, L23

Ferland, G., *et al.* 1995, in The Analysis of Emission Lines, edited by R. E. Williams and M. Livio (Cambridge University Press, Cambridge), p. 83

Graham, J. R., Herbst, T. M., Matthews, K., Neugebauer, G., Soiffer, B. T., Serabyn, E., & Beckwith, S. 1993, ApJ, 408, L105

Hajian, A. R., Terzian, Y., & Bignell, C. 1993, AJ, 106, 1965

Hayes, D. S., & Latham, D. W. 1975, ApJ, 197, 593

Hoare, M. G., Roche, P. F., & Clegg, R. E. S. 1992, MNRAS, 258, 257

Hollenbach, D., & Natta, A. 1995, ApJ, 455, 133

Holtzman, J. A., Burrows, C. J., Casertano, S., Hester, J. J., Trauger, J. T., Watson, A. M., & Worthey, G. 1995, PASP, 107, 1065

Hummer, D. G., & Storey, P. J. 1987, MNRAS, 224, 801

Kaler, J. B. 1976, ApJS, 31, 517

Kawamura, J., & Masson, C. 1996, ApJ, 461, 282

Kim, S.-H., & Martin, P. G. 1996, ApJ, 462, 296

Kreysing, H. C., Diesch, C., Zweigle, J., Staubert, R., Grewing, M., & Hasinger, G. 1992, A&A, 264, 623

LeVan, P. D., & Rudy, R. J. 1983, ApJ, 272, 137

Masson, C. R. 1989, ApJ, 346, 243

Mathis, J. S., Rumpl, W., & Nordsieck, K. H. 1977, ApJ, 217, 425

Miller, J., & Mathews, W. G. 1972, ApJ, 172, 593

Moseley, H., & Silverberg, R. F. 1985, in Airborne Astronomy Symposium, edited by H. A. Thronson and E. F. Erickson, NASA Conf. Pub. No. 2353 (NASA, Washington, DC), p. 233

O'Dell, C. R. 1963, ApJ, 138, 1018

O'Dell, C. R., & Terzian, Y. 1970, ApJ, 160, 915

Peimbert, M. & Torres-Peimbert, S. 1971, Boln. Obs. Tonantzintla Tacubaya, 6, 21

Preite-Martinez, A., & Pottasch, S. R. 1983, A&A, 126, 31

Pwa, T. H., Pottasch, S. R., & Mo, J. E. 1986, A&A, 164, 184

Rouleau, F., & Martin, P. G. 1991, ApJ, 377, 526

Rudy, R. J., Cohen, R. D., Rossano, G. S., Erwin, P., Puetter, R. C., & Lynch, D. K. 1991, ApJ, 380, 151

Seaton, M. J. 1979, MNRAS, 187, 73P

Shupe, D. L., Larkin, J. E., Knop, R. A., Armus, L., Matthews, K., & Soifer, B. T. 1997, ApJ (in press)

Siebenmorgen, R., Zijlstra, A. A., & Krügel, E. 1994, MNRAS, 271, 449

Taylor, A. R., Gussie, G. T., & Pottasch, S. R. 1990, ApJ, 351, 515

Whitford, A. E. 1958, AJ, 63, 201

© American Astronomical Society • Provided by the NASA Astrophysics Data System

1997AJ....113.2147H

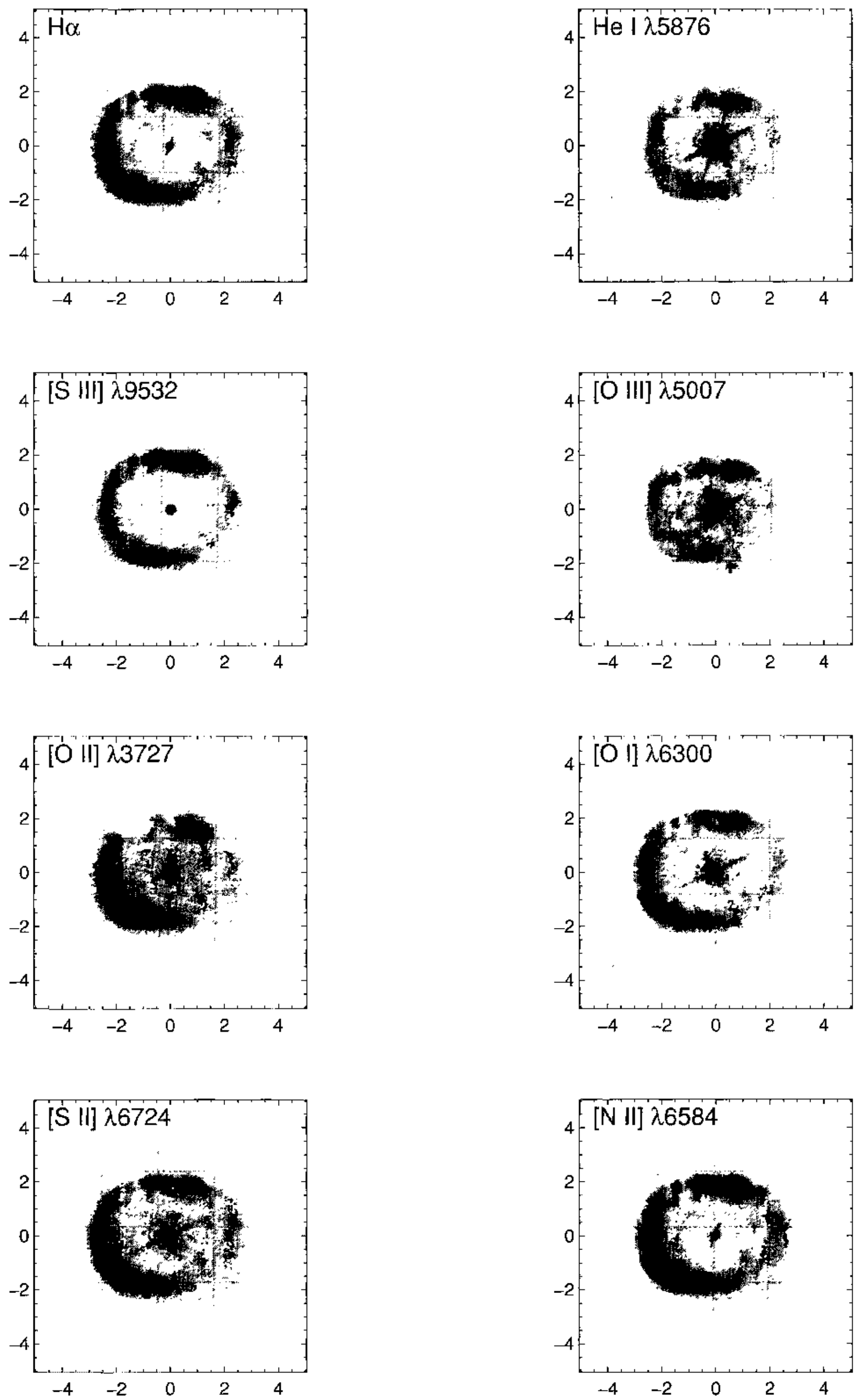

FIG. 1. Images of BD +30°3639 taken with the *HST* WFPC2. North is up and east is to the left. The axes are labeled in seconds of arc. The intensity scale is linear.

(see page 2147)

© American Astronomical Society • Provided by the NASA Astrophysics Data System

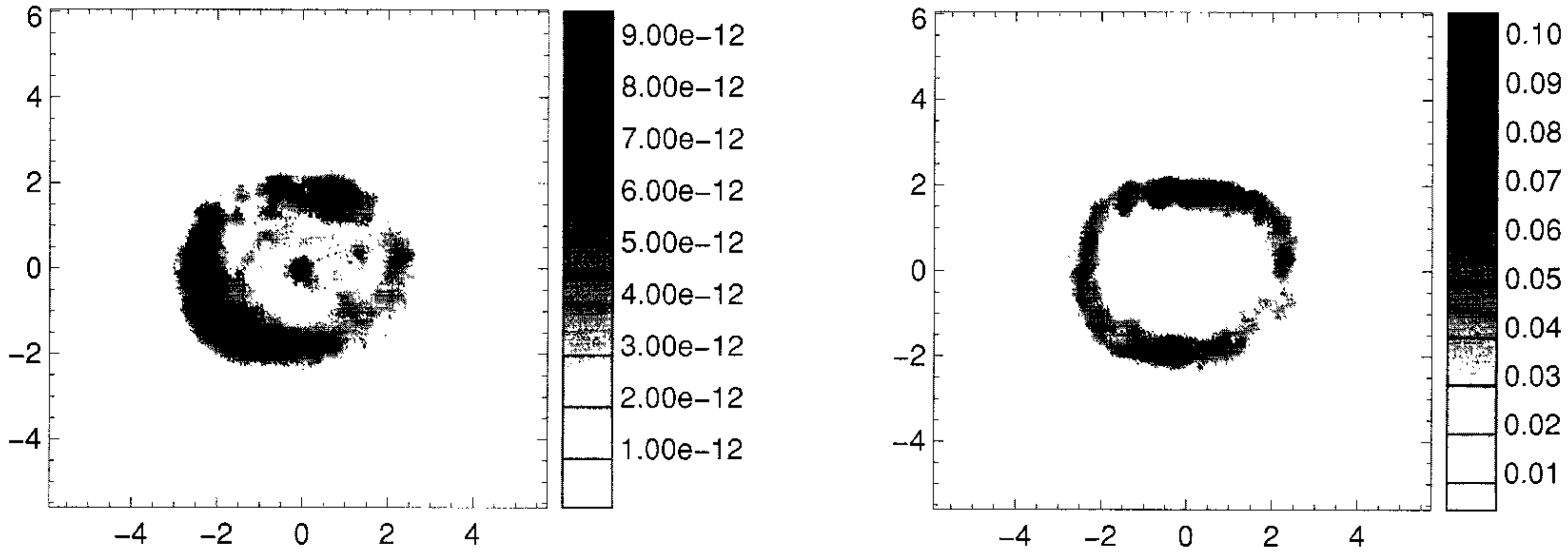

FIG. 5. The *HST* WFPC2 Hβ image of BD +30°3639 (*left*) compared to the VLA radio map (*right*). The axes are labeled in arcsec. The intensity scale of the Hβ image is in ergs cm^{-2} s^{-1} arcsec^{-2}, and that of the radio map in Jy arcsec^{-2}.

(see page 2150)

© American Astronomical Society • Provided by the NASA Astrophysics Data System

1997AJ....113.2147H

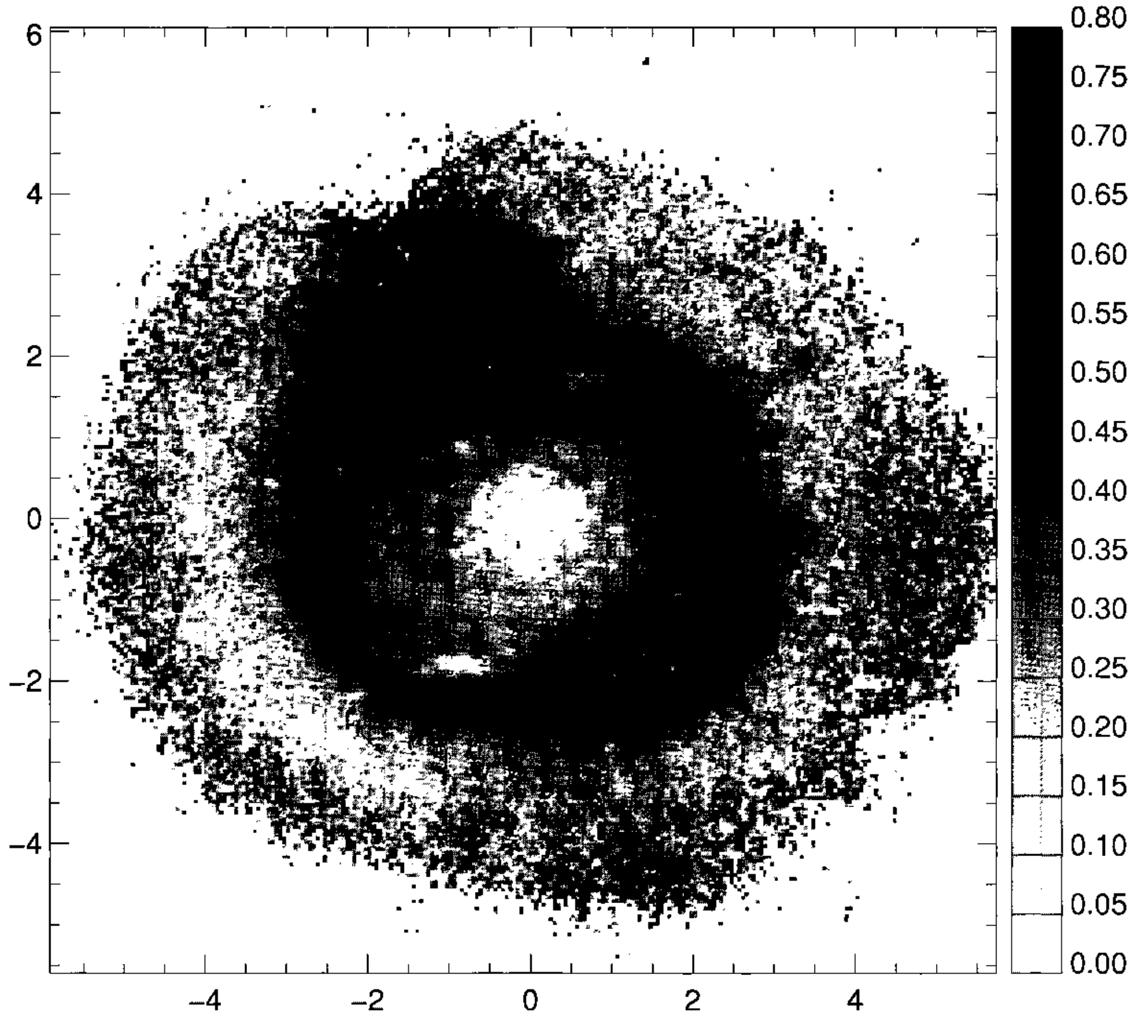

FIG. 6. The selective extinction $E_{\beta-\alpha}$ as defined by Eq. (2) in the text, after removal of the presumed ISM component.

(see page 2151)

© American Astronomical Society • Provided by the NASA Astrophysics Data System

1997AJ....113.2147H

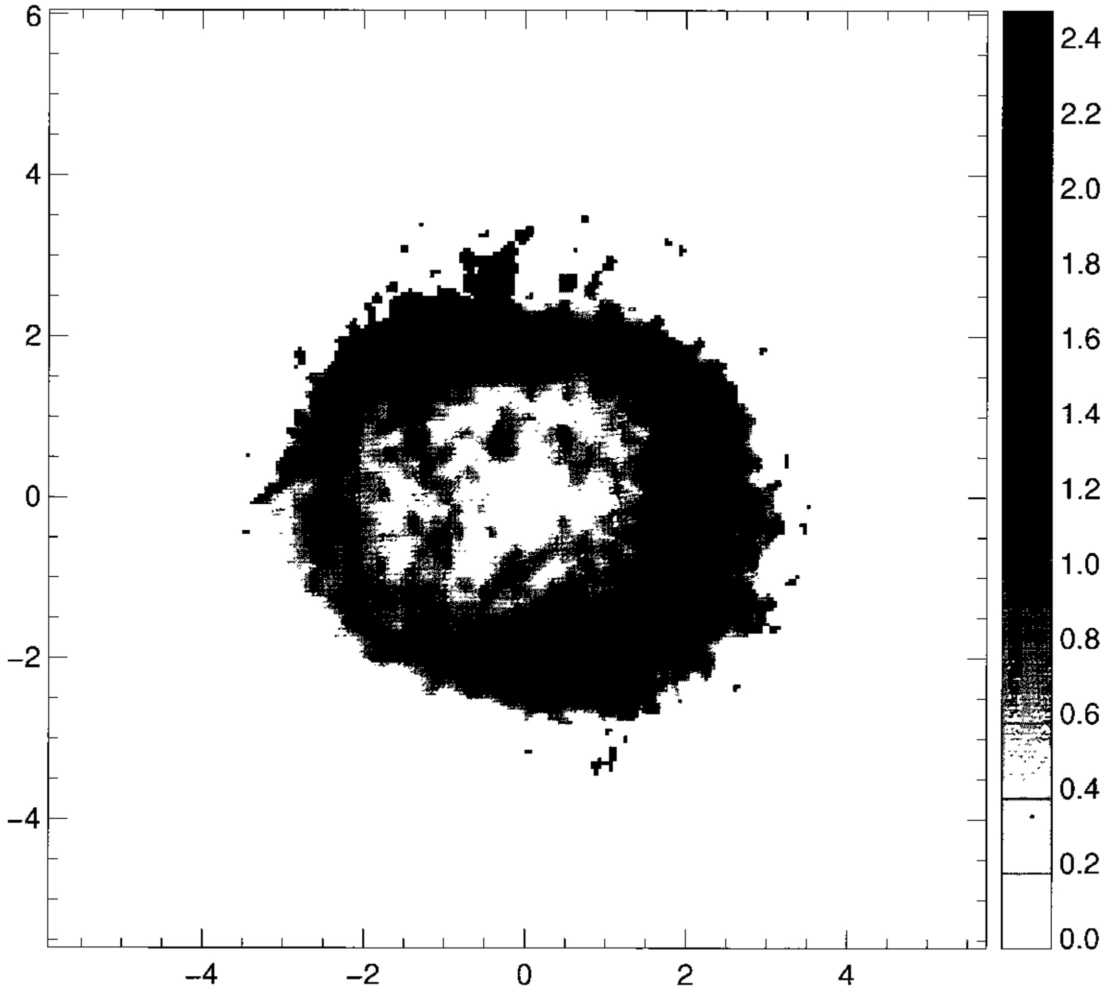

FIG. 7. The total extinction A_β as defined by Eq. (3) in the text, after removal of the presumed ISM component.

(see page 2151)

© American Astronomical Society • Provided by the NASA Astrophysics Data System

1997AJ....113.2147H

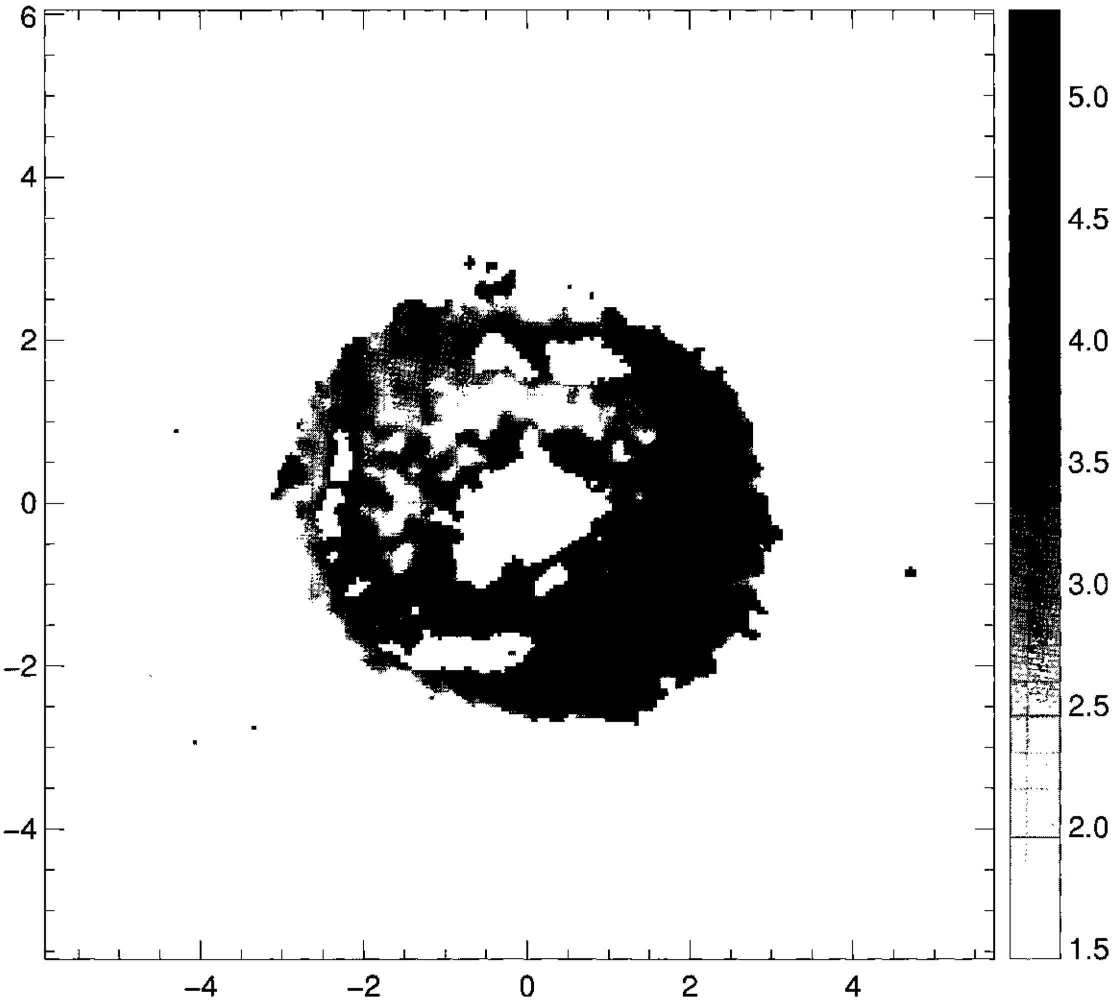

FIG. 8. The ratio of total to selective extinction, $R_{\alpha,\beta}$. Regions of very low radio flux near the central star and regions where Hα is saturated have been masked out.

(see page 2152)

© American Astronomical Society • Provided by the NASA Astrophysics Data System

1997AJ....113.2147H

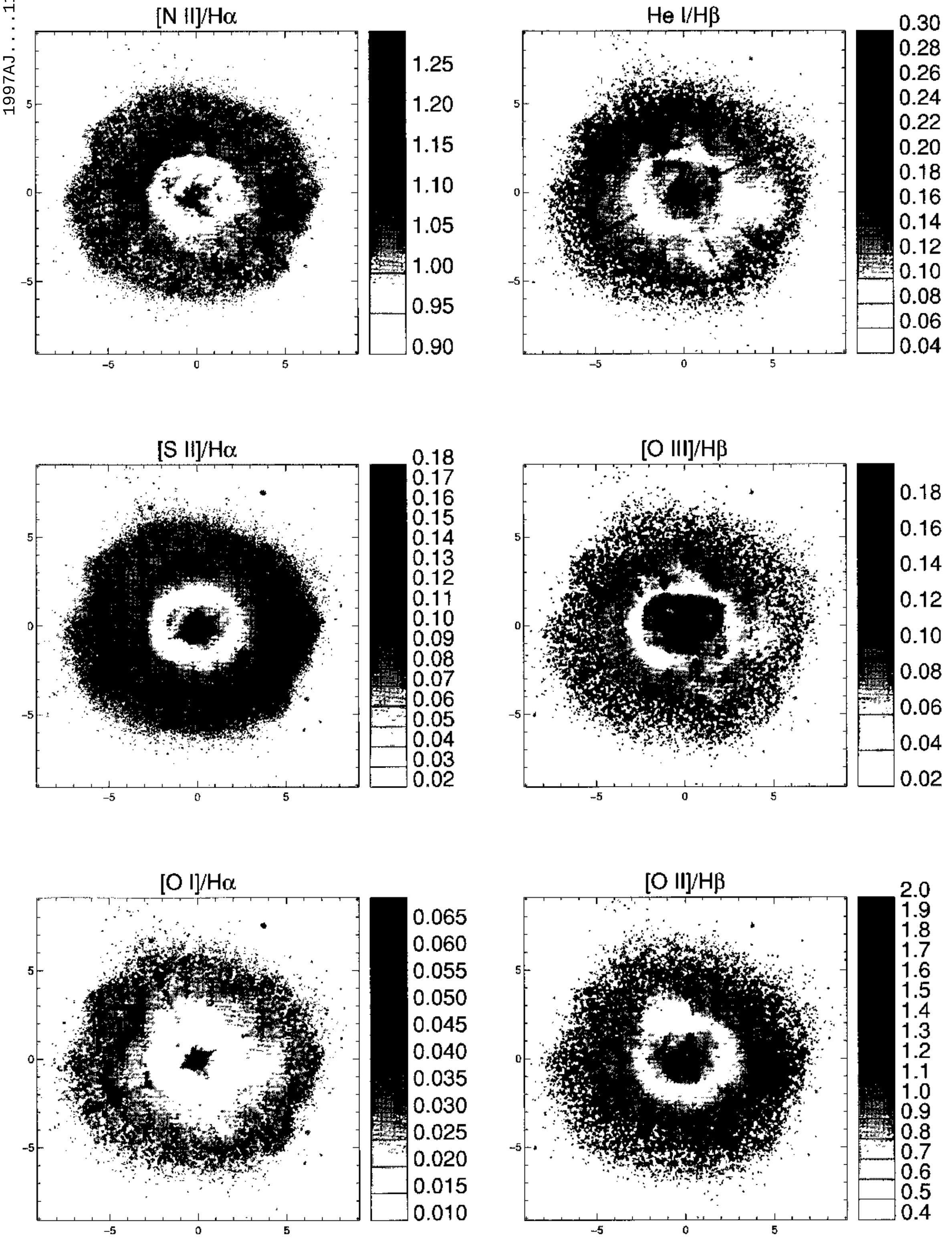

FIG. 14. Ratio maps of six emission lines relative to Hα or Hβ (whichever is nearest in wavelength).

(see page 2154)

© American Astronomical Society • Provided by the NASA Astrophysics Data System